



UNIVERSITÀ POLITECNICA DELLE MARCHE
Repository ISTITUZIONALE

Experimental crack identification of API X70 steel pipeline using Improved Artificial Neural Networks based on Whale Optimization Algorithm

This is the peer reviewed version of the following article:

Original

Experimental crack identification of API X70 steel pipeline using Improved Artificial Neural Networks based on Whale Optimization Algorithm / Ouladbrahim, A.; Belaidi, I.; Khatir, S.; Magagnini, E.; Capozucca, R.; Abdel Wahab, M.. - In: MECHANICS OF MATERIALS. - ISSN 0167-6636. - STAMPA. - 166:(2022).
[10.1016/j.mechmat.2021.104200]

Availability:

This version is available at: 11566/294023 since: 2024-06-07T11:17:39Z

Publisher:

Published

DOI:10.1016/j.mechmat.2021.104200

Terms of use:

The terms and conditions for the reuse of this version of the manuscript are specified in the publishing policy. The use of copyrighted works requires the consent of the rights' holder (author or publisher). Works made available under a Creative Commons license or a Publisher's custom-made license can be used according to the terms and conditions contained therein. See editor's website for further information and terms and conditions.

This item was downloaded from IRIS Università Politecnica delle Marche (<https://iris.univpm.it>). When citing, please refer to the published version.

(Article begins on next page)

Experimental crack identification of API X70 steel pipeline using improved Artificial Neural Networks based on Whale Optimization Algorithm

by

Abdelmoumin Ouladbrahim¹, Idir Belaidi¹, Samir Khatir², Erica Magagnini³, Roberto Capozucca³,
Magd Abdel Wahab^{4,5}

ABSTRACT

Intelligent systems have recently received recognition for their ability to solve extremely complicated and multidimensional problems. Artificial Neural Networks (ANN) has quite a lot of success in overcoming such issues, but some limitation can be found. The present study discusses in detail the application of the WOA-ANN hybrid model for predicting the crack length based on different input values, i.e. strains, stresses, and displacements, to test the accuracy of the presented technique. The proposed technique is compared with GA-ANN, AOA-ANN, and WOABAT-ANN. Coupled metaheuristic optimization algorithms with ANN aim to increase its efficiency. The connectivity between neurons carries some weight. Neurons are also connected to some biases. Connection weights and biases are modified to give the smallest possible error function based on the input values, and corresponding target output values supplied. Back Propagation (BP) is the usual name for this approach. The investigated approach is related to real engineering applications and controls the structures' state. Standard ASTM test specimens are chosen to study the evolution of fracture mechanics parameters. Next, an analytical model is developed by simulating the tests using the Finite Element Method (FEM) and validated with experimental results. FEM is used to analyse the tensile failure process of the one-sided notch samples with the mesoscopic GTN damage model and extract the data required for WOA-ANN. After collecting the database, our model is

¹ LEMI Laboratory, Department of Mechanical Engineering, University M'hamed Bougara Bumerdes, 35000 Bumerdes, Algeria

² Faculty of Civil Engineering, Ho Chi Minh City Open University, Ho Chi Minh City, Viet Nam
Samir.khatir@ou.edu.vn ; Khatir_samir@hotmail.fr

³ DICEA, Structural Section, Polytechnic University of Marche, Ancona, Italy

⁴ Institute of Research and Development, Duy Tan University, 03 Quang Trung, Da Nang 550000, Viet Nam

⁵ Soete Laboratory, Faculty of Engineering and Architecture, Ghent University, Technologiepark Zwijnaarde 903, B-9052 Zwijnaarde, Belgium

ready for predicting different scenarios. The obtained results using WOA-ANN are efficient compared to other techniques.

Keywords: GTN damage Model; GA-ANN; AOA-ANN; WOA-BAT-ANN; WOA; Crack identification.

1. Introduction

Structural Health Monitoring (SHM) of pipeline structures is of great interest and constitutes a fundamental element for the transport of hydrocarbons. API 5L X70 is among the steels used for construction (Ouladbrahim et al., 2021a), which occupies a very important place in the mechanical, naval and especially oil industry. High-strength steel pipelines allow the transportation of oil and gas at high pressure to increase the capacity, because the thickness of the pipes can be reduced when the strength of the steel of the pipeline is increased, and then the weight can be reduced. In the pipeline industry, pipes need high strength and durability as well as formability, which are important components, as mentioned in Refs. (Xie et al., 2021; Cabrini et al., 2015). The high strength and durability of steel allow natural gas and crude oil to be transported over long distances and under high pressure (Bott et al., 2005). The resistance of cracking due to hydrogen is an important property, which is added to other properties in an acid medium as described in Ref. (Sha and Li, 2016; Shi et al., 2016). In the H₂S environment problem, resistance to stress corrosion cracking was studied in Refs (Mohtadi-Bonab et al., 2013; Contreras et al., 2005). and the phenomenon of fatigue in Refs.(Han et al., 2012; Zhong et al., 2006). The chemical composition of metal alloys and thermomechanical processing has been shown to affect the properties and microstructure of the steel of the transport pipeline (Sun et al., 2002). Ensuring the integrity of large structures and industrial components involves considering the presence of faults and determining the conditions for initiating, propagating, and stopping cracks due to the presence of these faults (Capozucca and Magagnini, 2018, 2020). In order to identify this propagation phenomenon, we analysed the evolution of the crack within the framework of the elastoplastic fracture mechanics (Nilsson et al., 2010). It consists essentially of experimental tests and numerical simulations to allow the measurement of critical fracture properties from samples at the laboratory scale and to reduce the critical value of the fracture energy. More information can be found in the text books (Broek, 2012; Cruse, 2012; François et al., 2012). Other works are oriented towards the practical use of fracture mechanics (Hertzberg et al., 2020; Antolovich et al., 2018). A good suitable design

of tubes in terms of weight and strength requires advanced and high strength materials, and more details can be found in Ref. (Noell et al., 2018). At the beginning of the development of the failure model, the emphasis was placed on the triaxiality of the constraints and since the in-depth experimental studies. There is a trend within the natural gas transportation industry towards lower operating pressures, temperatures, and the use of higher quality pipeline materials (Fang et al., 2015). Moreover, the emergence of these changes in characteristics has come to a great need to accurately predict the stopping behaviour of ductile fracture in metal under these conditions. However, many experts believe that forecasting methods found in the industry require significant improvement, as they are suitable for lower grades of steel and lower operating pressures by the standards of the operating environment as described in Ref. (Rudland et al., 2004). In the pipeline, there are two types of crack, namely ductile crack, and brittle crack. Since ductile crack occurs at a higher temperature where virtually all pipelines are in service. In pipeline industry applications, it is important to control the propagation and stop the ductile cracks. An elastic crack propagates unstably for a long time as the crack velocity is less than the decompression rate during initial compression. This is because the decompression rate and crack rate decrease as pressure decreases at the bottom crack (Nakai et al., 2016). The damage model of GTN is widely applied to simulate the dynamic propagation of ductility fractures. Due to the limited set of parameters in this model, it is often adopted in engineering applications (Jackiewicz, 2011). The GTN mesoscopic damage model is used as a tool to support the FE model of the experimental test process. The provided results have shown that the fracture speed and the pronounced opening angle were in good agreement with the experimental results. Lian (Lian et al., 2018) simulated the failure process of an X70 high steel pipeline under loading conditions and established a damage mechanics model with hole expansion being a damage variable. Gholipour et al. (2019) presented an application based on the GTN damage model, the model simulates with acceptable precision of material fracture and damage evolution for SAE 1010 plain carbon steel. Recently, ANN has been widely used for different applications, such as surface texture, mechanical properties, the effects of processing

parameters on the alteration of mechanical properties, the phenomenon of corrosion and fatigue, damage identification (Khalaj et al., 2013; O'zel and Karpas, 2005; Brahme et al., 2009; Ouladbrahim et al., 2021b; Zenzen et al., 2020). Besides, ANN was improved based on some challenges using optimization techniques for damage identification in several structures as mentioned in Refs. (Khatir et al., 2020, 2021; Seguni et al., 2021).

In this paper, the application of GTN damage is developed to predict ductile fracture in the case of tensile tests including different crack lengths. The tensile fracture simulations are used to model a high-strength pipe material, namely API X70. The numerical model results are utilized to construct results based on different outputs (strains, stresses, and displacements). Next, the investigated results are compared with experimental ones for validation. The provided results are collected for WOA-ANN techniques to predict the crack lengths compared with GA-ANN, AOA-ANN, and WOA-BAT-ANN. The objective of hybrid optimization techniques is to improve the bias and weight parameters for better results.

2. GTN model constitutive description

Plastic damage is the process of plastic deformation until fracture. The damage mechanism denotes the damage evolution process of the micro-hole formed by the internal inclusions or two-phase particles of the metal being nucleated, growing up, and converging under external forces. In order to describe the mechanism of meso-damage of plastic materials and its evolution process, a suitable model should be established as presented in Ref (Xue, 2007). Gurson (Aldakheel et al., 2018), based on McClintock, Rice, and Tracey (Aldakheel et al., 2018), assumed that plastic deformation of the material is mainly caused by micro-hole damage. Gurson (Jiang et al., 2016) did not use the assumption of the infinite matrix, but proposed a finite matrix with a microporous cell model. Next, Tvergaard and Needleman have modified some parameters of the Gurson model, which significantly improved its prediction with more accuracy in Ref (Li et al., 2015). The Gurson yield surface function corrected by Tvergaard and Needleman as presented in the following formulation:

$$\Phi = \left(\frac{\sigma_{eq}}{\sigma_e} \right)^2 + 2q_1 f^* \cosh \left(\frac{3q_2 \sigma_m}{2\sigma_e} \right) - (1 + (q_1)^2 f^{*2}) = 0 \quad (1)$$

where σ_{eq} denotes the macroscopic Von Mises equivalent stress; σ_e is the yield stress of the base metal in the element; σ_m is the macroscopic mean stress, and f is the pore volume fraction. q_1, q_2, q_3 are the correction parameters taking into account the micro-hole around the non-uniform stress field and the adjacent holes in the middle of the interaction, which are usually taken equal to $q_3=q_1^2$, $q_1=1.5, q_2=1.0, q_3=2.25$.

$$f^* = \begin{cases} f \\ f_c + \frac{f_u^* - f_c}{f_F - f_c} (f - f_c) \\ f_u^* \end{cases} \rightarrow \begin{cases} f \leq f_c \\ f_c < f < f_F \\ f \geq f_F \end{cases} \quad (2)$$

In the above formula, f^* is the equivalent void volume fraction, which explains the gradual decrease of the bearing capacity of the material due to pore polymerization; f_c is the pore volume fraction at the time when the hole starts to polymerize; f_F is the broken void volume fraction when the material is destroyed; $f_u^* = 1/q_1$ is the limit void volume fraction when the stress-bearing capacity is zero. The evolution of void volume fraction, f^* , can be considered as a combination of existing void growth, f_{growth}^* , and nucleation of new voids, $f_{nucleation}^*$:

$$f^* = f_{growth}^* + f_{nucleation}^* \quad (3)$$

Void growth can be written as a function of the rate of plastic volume change, ε_{kk}^{pl} :

$$f_{growth}^* = (1 - f) \dot{\varepsilon}_{kk}^{pl} \quad (4)$$

Void nucleation is defined in a strain-controlled nucleation function that considers a normal distribution for the nucleation strain. Consequently, the void nucleation rate can be written as:

$$f_{nucleation}^* = \frac{f_n}{S_n \sqrt{2\pi}} \exp \left[-\frac{1}{2} \left(\frac{\bar{\varepsilon}^{pl} - \varepsilon_n}{S_n} \right)^2 \right] \dot{\varepsilon}^{pl} \quad (5)$$

where f_n defines the void volume fraction of nucleated voids, ε_n and S_n indicate the mean value and standard deviation of the nucleation strain, respectively, $\bar{\varepsilon}^{pl}$ indicates the equivalent plastic strain

and $\dot{\bar{\epsilon}}^p$ defines the equivalent plastic strain rate. Finally, the initial void volume fraction f_0 denotes the presence of initial voids and is a measure for the relative density of the material. In this investigation, the GTN damage parameters, listed in Table 1, are considered as typical material constants as obtained in Ref (Jang et al., 2019; Ouladbrahim et al., 2021a). The plasticity based on the true stress-strain relations can be shown in Fig. 1.

Table 1 - GTN damage parameters for API X70.

GTN damage parameters for API X70.

f_c	f_n	f_0	f_F	ϵ_n	S_n	q_1	q_2
0.019	0.005	0.00015	0.18	0.3	0.1	1.5	1

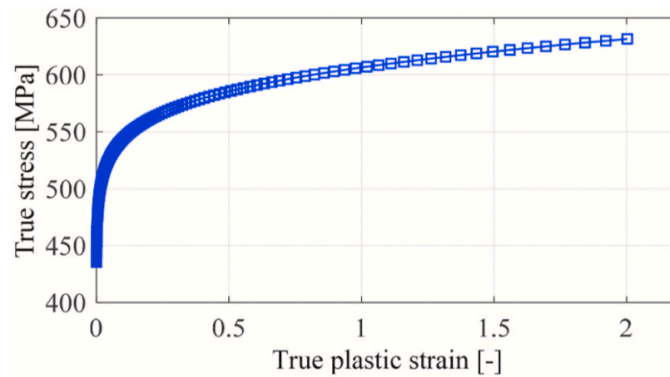


Figure 1 - True stress-strain curve for API X70.

3. Numerical models

FE model of the tensile test of base metal is constructed using ABA- QUS software. A 3D solid FE model was implemented in order to reproduce the fracture tensile experiment in a laboratory scale test.

ABAQUS explicit solver allowed the application of the GTN damage model for the simulation of dynamic crack propagation. For this pur- pose, a model called “porous metal plasticity” is used.

The geometry was created based on the standard dimensions of the specimen (ASTM). In each model, the mesh was created using an eight- node linear brick (C3D8R).

The accuracy of the numerical calculation is strongly linked to the quality of the mesh around at the crack tip. The mesh size has more significant importance when the GTN damage model is used. In this study, the element size is 0.2. Using the data from the results of the previous uniaxial tensile tests, we have implemented the materials plasticity properties as shown in Fig. 1. The boundary conditions in the numerical model is fixed in the bottom end including all degree of freedom (DOF). Next, The other side at the top of the model is allowed to move only in the direction of the load in the y-axis, as shown in Fig. 2.

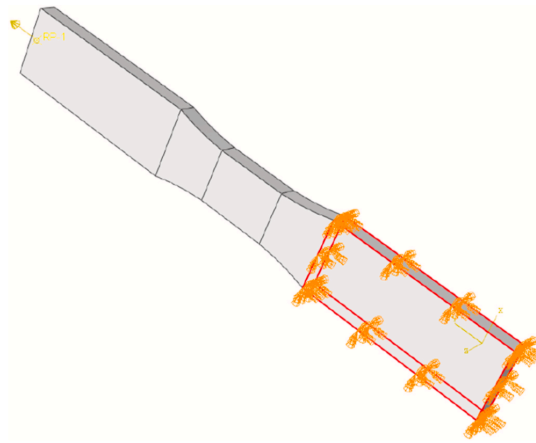


Figure 2 - Boundary conditions for the modeled tensile test specimens of base metal.

In this section, the numerical simulation is performed to be used for different crack lengths in the critical zone. The refinement mesh is considered where the high-stress concentration is expected, in particular at the interface as indicated in Fig. 3-a. The dimensions of the specimen are presented in Fig. 3-b.

3.1. Load-displacement simulation curve

Based on the experimental results, the obtained load-displacement curve from FE simulation in ABAQUS is plotted in Fig. 4. Three regions are considered in this curve: I-before the yield point, II-between the yield point and the ultimate point, and III-after the maximum point till the final fracture. All points P1, P2, P3, and P4, are represented in Fig. 4.

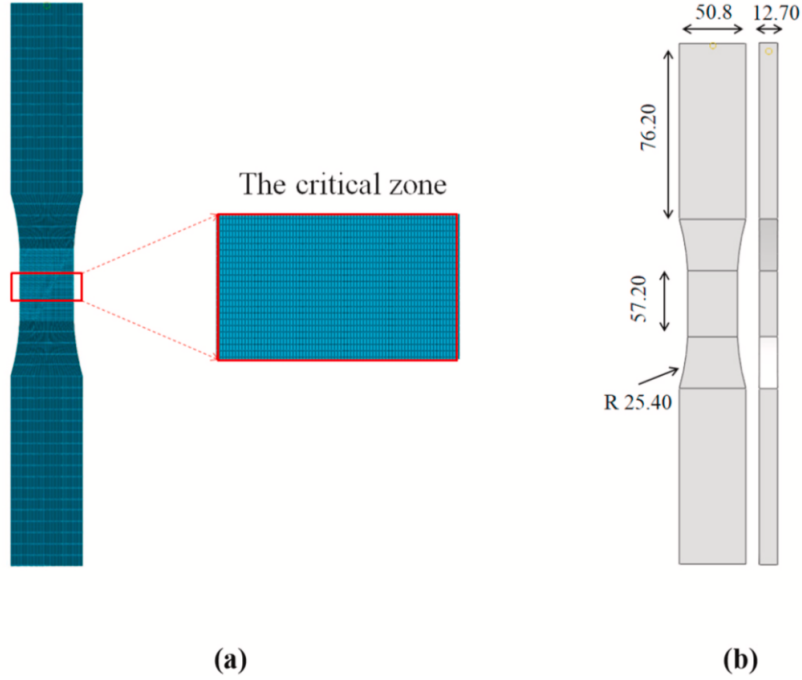


Figure 3 - a- Mesh refinement in the critical zone b-The geometry.

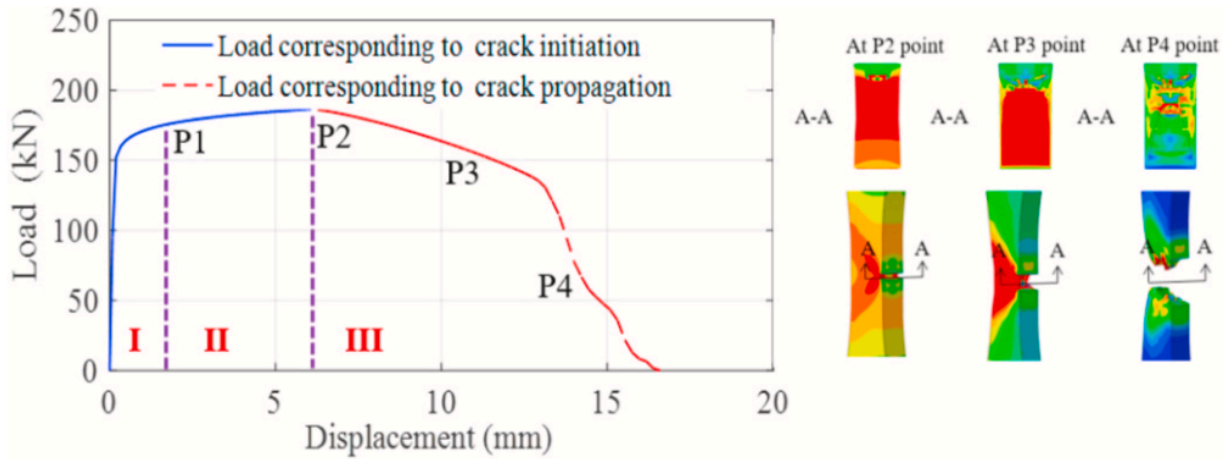


Figure 4 - Simulated load-displacement curve of single edge crack of API X70.

In Fig. 4, firstly, in region I, the load increases linearly with the displacement to the yield point P1, and the material API X70 steel deforms plastically. Secondly, in region II, between P1 and P2, the load with the displacement continuously increases. Thirdly, in region III, the necking is observed and is represented by the specimen area reduced to the final separation observed at P4. Crack behavior is presented based on experimental analysis using a camera at different times see Fig. 5-a.

A good agreement of the specimen geometries predicted in the simulation based on stress contours is presented in Fig. 5-b.

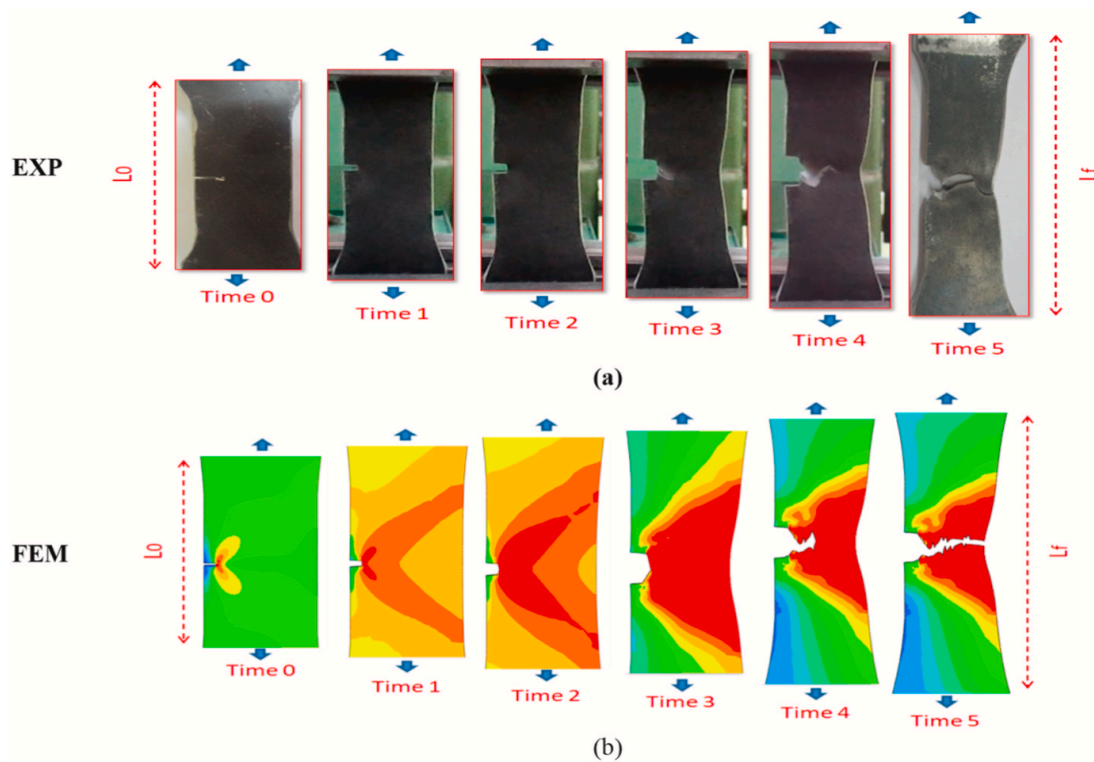


Figure 5 - Fracture process of API X70 steel during the test: Experiment (a) and FE simulation (b).

4. Experimental tensile test of pipeline steel

4.1. The tensile test of a specimen without crack

The material of our study is a manganese carbon steel used for the transport of hydrocarbons under a working pressure of 70 bars with the name API X70. In order to determine the load displacement curves and the mechanical properties of API X70 steel, flat specimens according to standard NF EN 10002-1 (Bouledroua et al., 2017; Ouladbrahim et al., 2021a) were used under simple traction at room temperature in the tensile testing machine (ZwickRoell) at ALFAPIPE (Algerian manufacturing pipes laboratory) as shown in Fig. 6. The initial material is presented in coils of the same casting. The thickness of the test specimens and the geometrical dimensions of all the specimens are shown in Fig. 3-b.

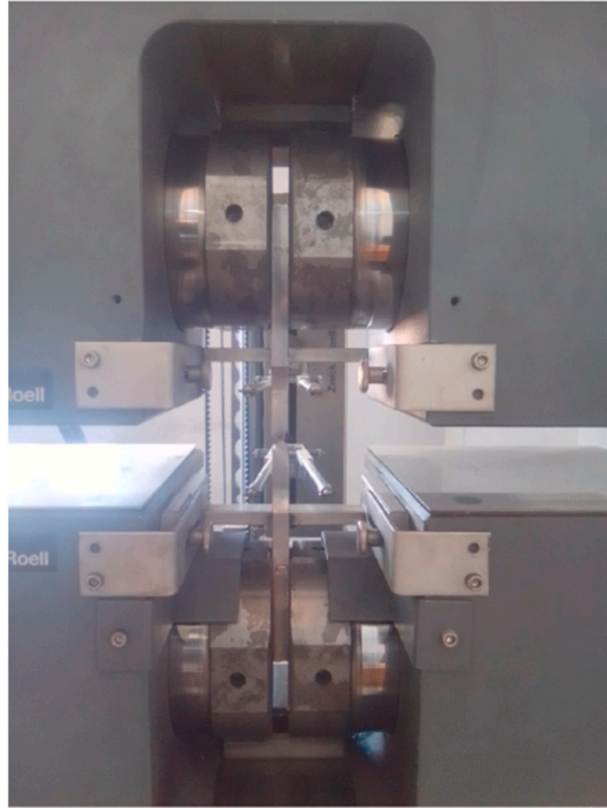


Figure 6 - Test specimen with a tensile extensometer in the tensile testing machine.

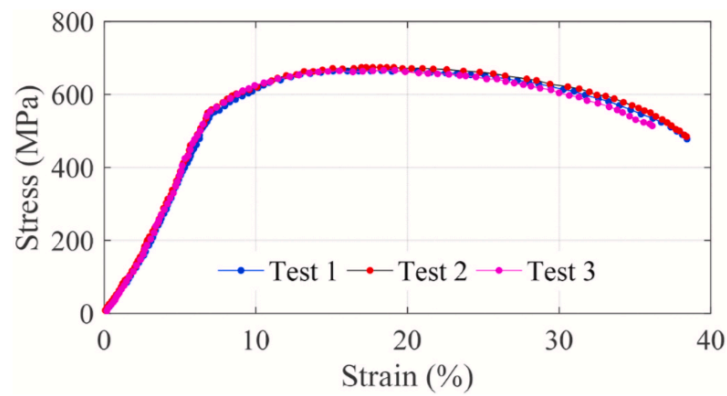


Figure 7 - Stress-strain diagrams of API X70 pipeline steel.

The experimental results for the tensile tests 1, 2, and 3 give the evolution of the stress according to the strain of the material as shown in Fig. 7. The general appearance of these curves shows ductile behaviour. Table 2 shows the mechanical properties of API X70 pipeline steel, which can be used for numerical simulation, with E Young's modulus, ν Poisson's ratio, YS yield strength according

to the standard. UTS is the ultimate tensile strength, EL% is the elongation at break, and k and n are the parameters of Hollomon.

Table 2 - Mechanical properties of API X70 steel.

E (MPa)	ν	Yield strength YS (MPa)	Ultimate tensile strength UTS (MPa)	Elongation EL %	k	n
$2.10 \cdot 10^5$	0.3	558	672	38	850	0.095

The tensile tests were carried out using a Zwick/Roell materials testing machine type tensile machine, which is directly connected with a computerized system for the acquisition of experimental data.

After evaluating the test data provided in “API X70 tensile test”, the variation of the load F as a function of the displacement ΔL , is obtained as shown in Fig. 8.

Comparison between experimental and numerical results using the GTN model are shown in Table 3.

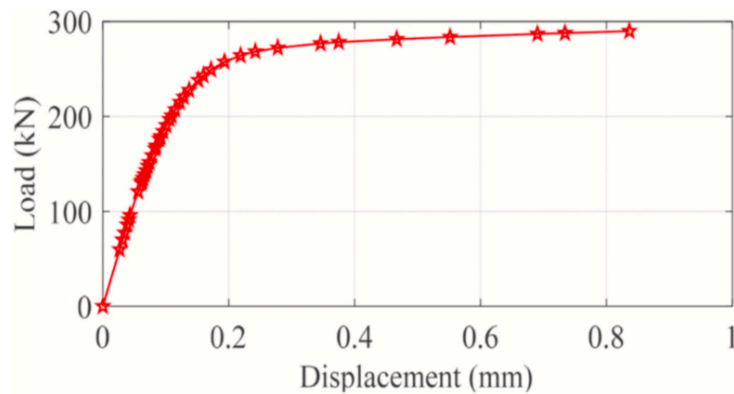


Figure 8 - Engineering load-displacement curves of the test data.

Table 3 - Comparison between the experimental and numerical results of the tensile test.

	YS (MPa)	UTS (MPa)	$(\Delta L)_u$ (mm)	ϵ_u (-)
Experimental (average between tests 1,2, and 3)	558	671	7.62	0.15
Simulation (GTN model)	547	659	6.75	0.135

4.2. The tensile test of a specimen with cracks

In this section, different crack lengths are considered, namely $L = 4, 7$, and 10 mm. Two specimens are tested for each crack length to obtain highly accurate results. To realize the test specimens, we have extracted a large plate that we have cut from the pipe. Next, a smaller plate is taken from this sample, one transverse to the shell, which contains only the base metal, see Fig. 9-b. The obtained plate is illustrated in Fig. 9-c.

To produce the specimens, a mechanical saw was used in order to cut the plate into two parts sufficient for the production of two specimens per plate. After cutting the plate, the specimens are manufactured by the milling process to obtain the specimens standard dimensions, see Fig. 10.

Next, different crack lengths, i.e. $4, 7$, and 10 mm, are cut as illustrated in Fig. 11.

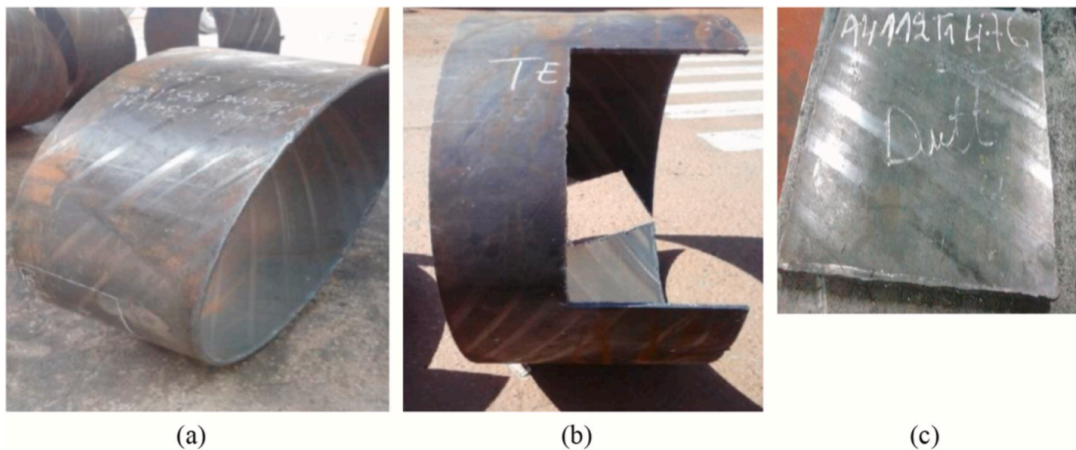


Figure 9 - A part of a pipe (a), Removal of the transverse base metal (b), and Plate “1” completely from base metal (c).



Figure 10 - Specimens used for tensile testing.

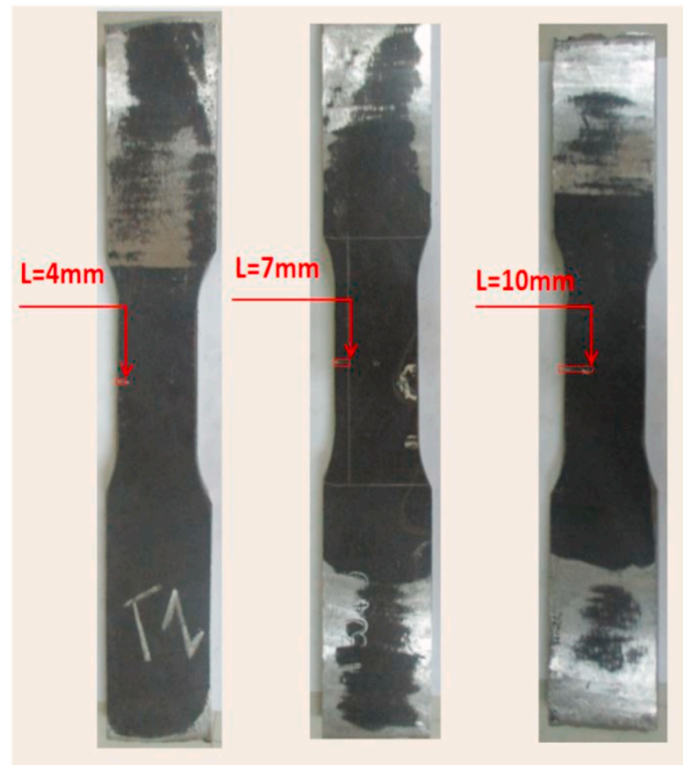


Figure 11 - Test specimens carried out for tensile tests according to different crack lengths.

The mechanical properties of the test specimen with three different crack lengths ($l = 4 \text{ mm}$, 7 mm , and 10 mm) from the experimental analysis and FEM results are presented in Table 4.

The obtained results in Table 4 are more effective, and the percent- age error between the experimental and FEM is less than 4.05% for test specimens with notches. Therefore, to better predict the crack length using WOA-ANN, more data are collected from the FE model for different crack lengths after validation.

Table 4 - Comparison between experimental and FEA stress results for different crack length.

	Yield Stress YS (Mpa)			Maximum Stress MS (Mpa)		
	Experimental Average (test 1-2)	FEM	% Error	Experimental Average (test 1-2)	FEM	% Error
$L = 4 \text{ mm}$	540	548	1.48	614	612	0.33
$L = 7 \text{ mm}$	505.5	514	1.68	574.5	563	2.00
$L = 10 \text{ mm}$	446	464	4.03	507	497	1.97

5. Improved Artificial Neural Network for crack prediction using WOA

Once an ANN is adequately trained, it can be used as a black-box model to link complex input and output datasets. Weights and biases connect the neurons together. The input layer, hidden layer, and output layer are the three layers of an ANN network. The hidden and output layers contain all neurons, while the input layer is devoid of them. Fig. 12 illustrates a typical ANN model.

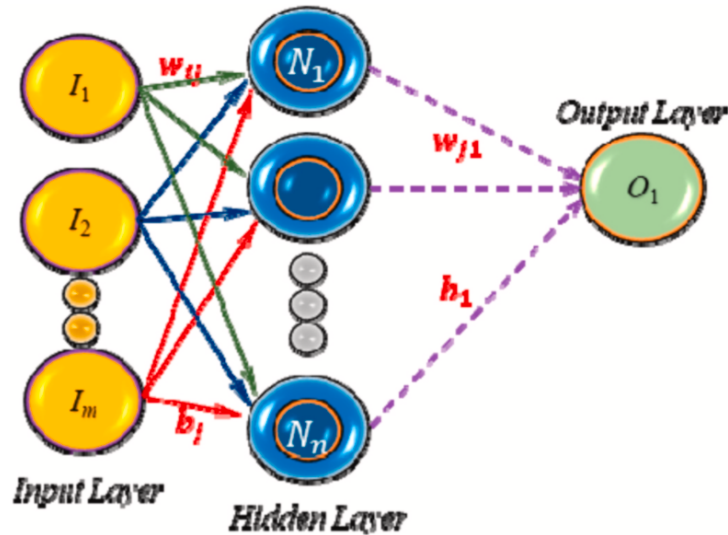


Figure 12 - A typical ANN architecture.

w_{ij} is the weights of neuron connection between i th input node and j th neuron in the hidden layers. b_j represents the bias associated with j th neuron in the hidden layer. w_j is the weight of neuron connection between j th neuron in a hidden and single neuron in the output layers. b_1 represents bias associated with the single neuron in output layer neuron. Indices $i=1,2,\dots,m$ and $j=1,2,\dots,n$ are input features and hidden layer neurons, respectively. The total number of parameters used in the network is $n*(m + 2) + 1$. Following the creation of the ANN model's structure, training with known input and output sets is carried out to determine the optimum weights and biases of the neurons. Various strategies are typically used to determine the optimum weights and biases for the ANN. In this study, MATLAB was used to perform optimum network training using WOA. Whales are creatures of fancy. They are considered as the world's largest mammals. Up to 30 m long and 180 tons weight, an adult whale can grow. This kind of Whale never sleeps because they have to breathe

from the ocean floor. Seven different species of this giant mammal exist, such as killer, Sei, humpback, Minke, finback, right, and blue. Whales are known mainly as predators. Half of the brain simply just sleeps. The remarkable thing about whales is that they are viewed with emotion as highly intelligent creatures. The location of prey can be recognized and encircled by humpback whales. The optimal design location in the search space is not known in advance. WOA assumes that the target prey is close to the optimum and is the current best candidate solution. Other search agents will then try to update their positions to the best search agent when it is identified. The following equations represent this behaviour:

$$\vec{D} = \left| \vec{C} \cdot \vec{X}^*(t) - \vec{X}(t) \right| \quad (6)$$

$$\vec{X}(t+1) = \vec{X}^*(t) - \vec{A} \cdot \vec{D} \quad (7)$$

where the latest iteration is defined by t , coefficient vectors are \vec{A} and \vec{C} , \vec{X} position vector, and \vec{X}^* is a position vector of the best solution obtained so far.

\vec{A} and \vec{C} can be calculated using the following formulations:

$$\vec{A} = 2\vec{a} \cdot \vec{r} - \vec{a} \quad (8)$$

$$\vec{C} = 2 \cdot \vec{r} \quad (9)$$

Then, a spiral equation is created to approximate the helix-shaped movement of humpback whales between the location of Whale and prey as presented in the following formulation:

$$\vec{X}(t+1) = \vec{D}' \cdot e^{bl} \cdot \cos(2\pi l) + \vec{X}^*(t) \quad (10)$$

where: $\vec{D}' = \left| \vec{X}^*(t) - \vec{X}(t) \right|$, (X, Y): Whale located. (X*, Y*): Prey located.

Humpback whales swim within a decreasing circle around the prey and along a spiral-shaped direction at the same time. Furthermore, to model this concurrent behaviour, we expect that there is

50% chance of choosing between either the shrinking encircling process or the spiral model to adjust the location of whales through optimization. The mathematical model is given as follows:

$$\vec{X}(t+1) = \begin{cases} \vec{X}^*(t) - \vec{A} \cdot \vec{D} & \text{if } p \geq 0.5 \\ \vec{D}' \cdot e^{bl} \cdot \cos(2\pi l) + \vec{X}^*(t) & \text{if } p < 0.5 \end{cases} \quad (11)$$

where p is a random number in $[0,1]$. For more details, the author may refer to Ref. (Mirjalili and Lewis, 2016).

The mathematical model is expressed as:

$$\vec{D} = \left| \vec{C} \cdot \vec{X}_{rand} - \vec{X} \right| \quad (12)$$

$$\vec{X}(t+1) = \vec{X}_{rand}(t) - \vec{A} \cdot \vec{D} \quad (13)$$

where \vec{X}_{rand} is a random position vector (a random whale) chosen from

the current population. More details about this algorithm can be found in Ref (Mirjalili and Lewis, 2016).

The objective function used to minimize root-mean-square error (RMSE) of the network, which is described in the following formulation:

$$RMSE = \sqrt{\frac{\sum_{l=1}^n (O_l - I_l)^2}{nd}} \quad (14)$$

where O_l denotes the output corresponding to l th data point in the training set by the network, I_l denotes the actual output as consider in the target set. nd is the number of data points used in the training dataset. The RMSE has been used as the objective function as mentioned of the ANN whose parameters (weights and biases) have to be optimised to improve the training. WOA is compared with GA, AOA, and WOA- BAT using different inputs. The number of collected data are 61 using different crack lengths from 4 mm to 34 mm.

5.1. Results and discussion

To study the effectiveness of WOA, different optimization techniques, such as GA, AOA, and WOA-BAT, are used with different inputs, such as stress, strain, and displacement, to adapt the weights and biases of ANN. The number of hidden layer sizes (Hidden neurons) is considered to select the adequate number using three scenarios with crack length 10 mm, 15 mm, 32 mm. The parameters used for all optimization techniques are 100 populations and 100 iterations. The characteristics of the computer used for the calculation are Intel(R) Core(TM) i7-6700HQ CPU @ 2.60 GHz 2.59 GHz and Ram Memory is 16 GB. The results are shown in Fig. 13.

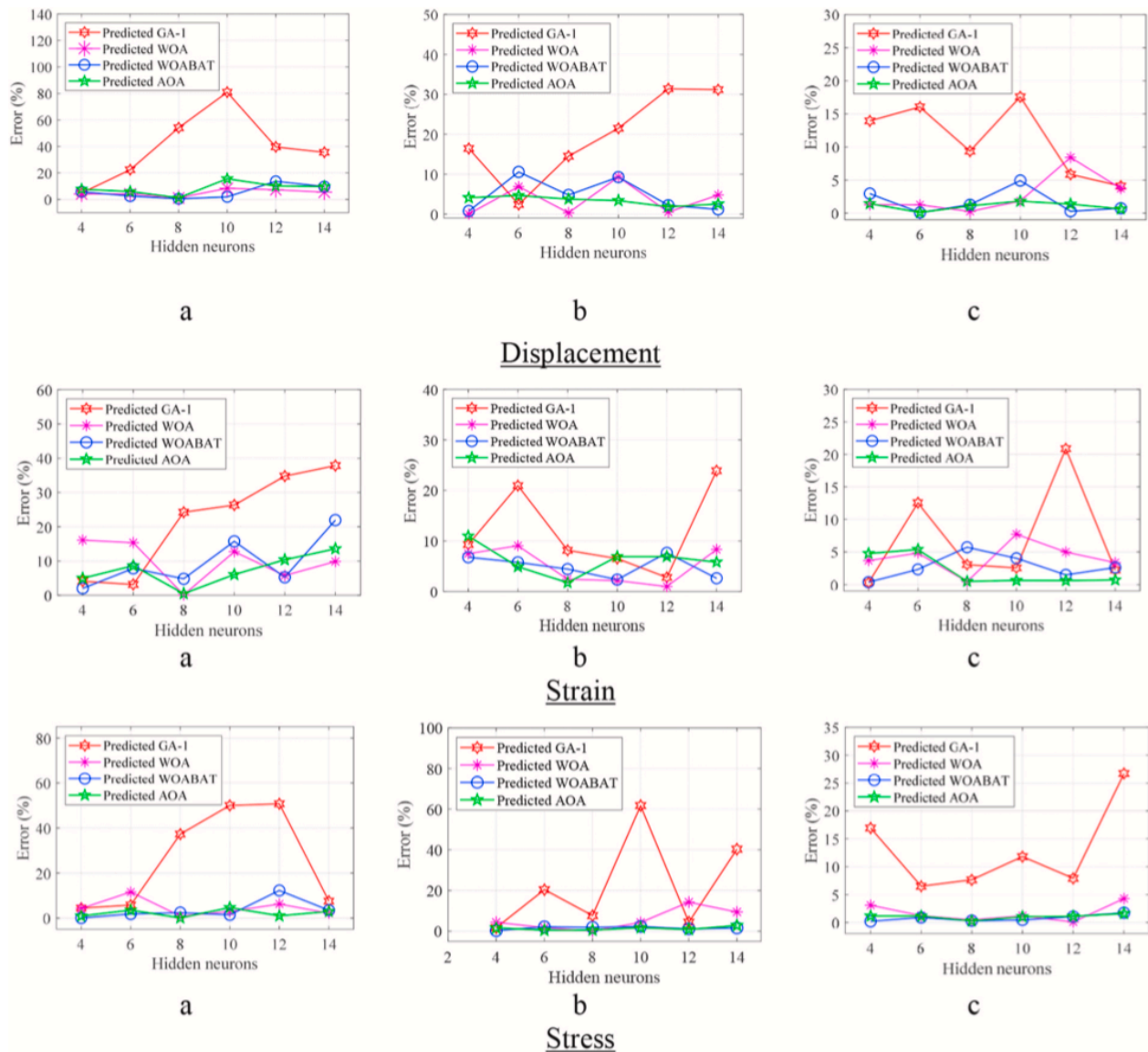
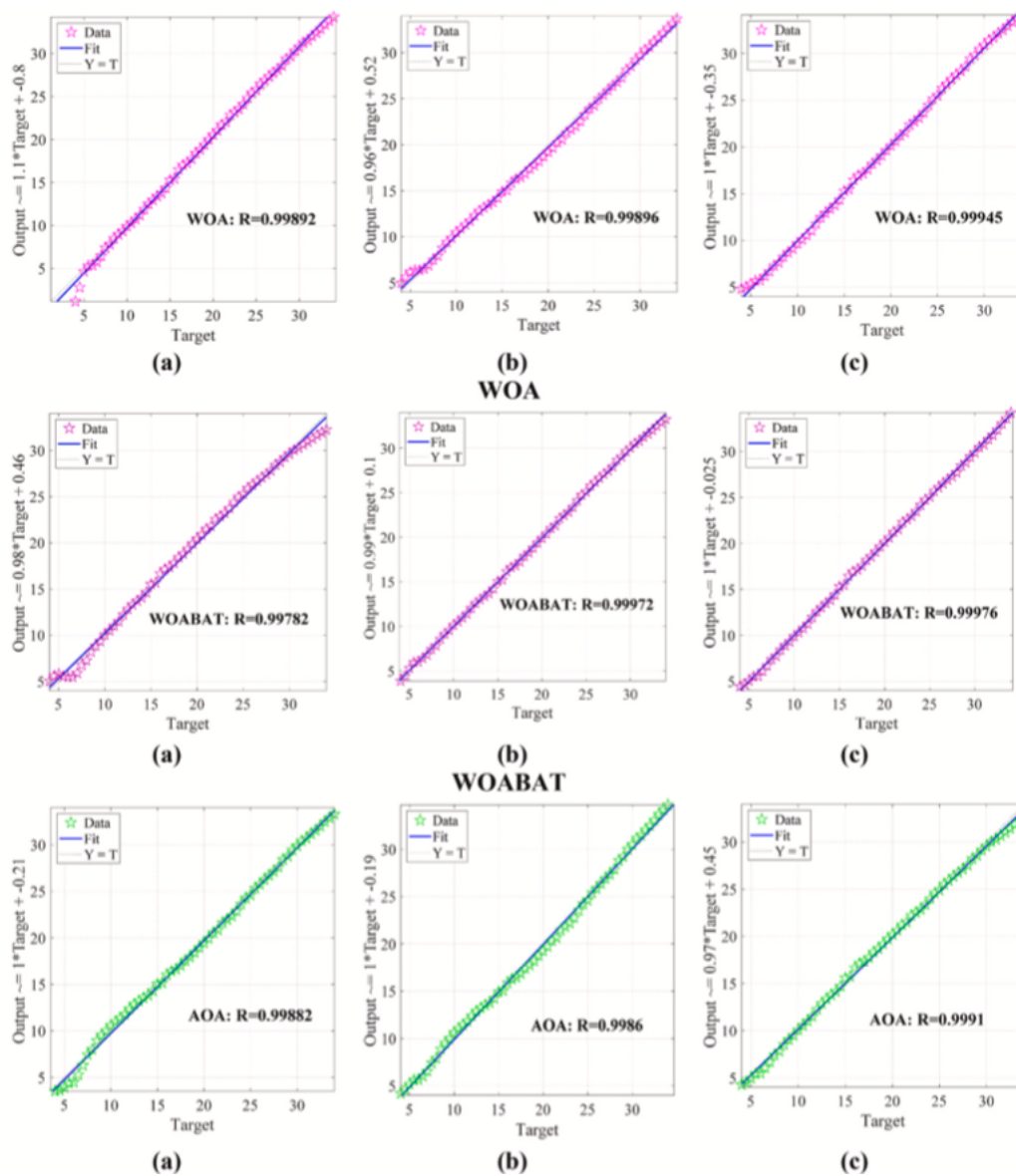
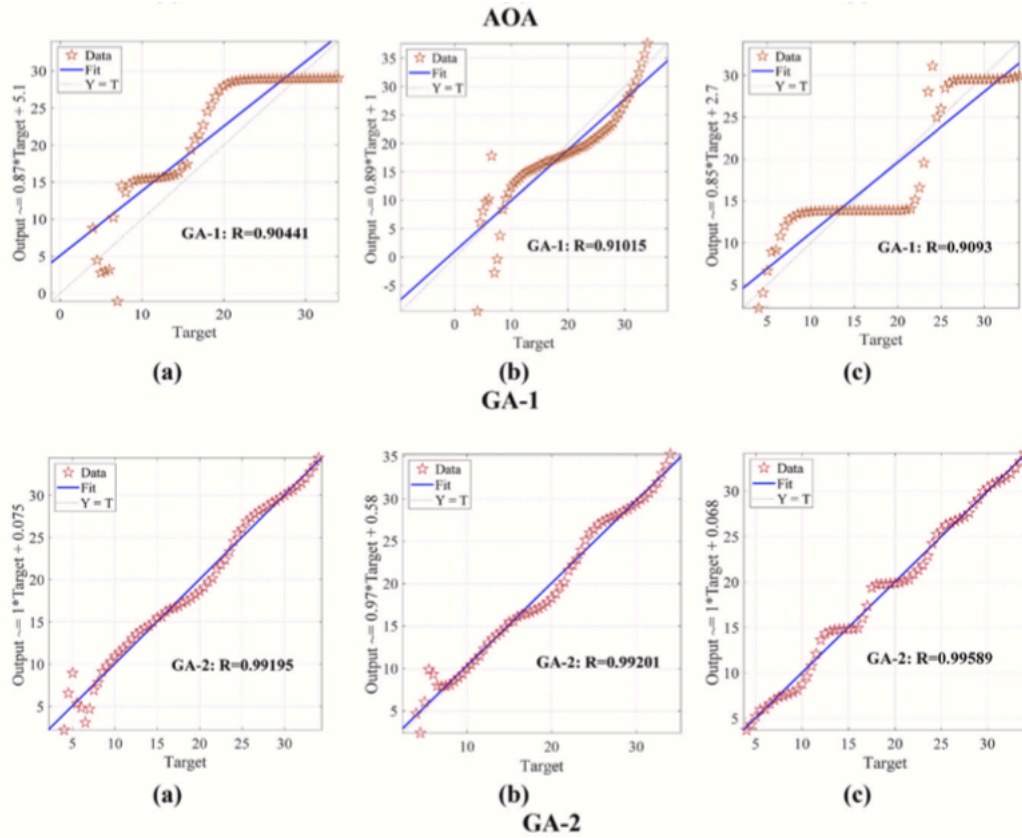


Figure 13 - Different hidden layer sizes (Hidden neurons) with different scenarios. Notation: Crack length: a = 10 mm, b = 15 mm, and c = 32 mm.

The results showed that the most optimum network obtained considering WOA, WOA-BAT, AOA, and GA combined with ANN has eight hidden neurons using different inputs based on the fitting examination. Next, five scenarios with actual crack lengths 10 mm, 15 mm, 24 mm, 28 mm, and 32 mm are considered using eight hidden neurons to predict the exact crack lengths. Based on the previous results, GA fails to predict the precise crack length. However, the population size is increased from 100 to 2000 after several tests. Fig. 14 shows the training performance of the best network using different inputs (displacement, strain and stress), including different optimization techniques.





Notation: GA-1: 100 populations-100 iterations, and GA-2: 2000 populations-100 iterations.

Figure 14 - Regression analysis: a) Displacement, b) Strain, c) Stress.

After the training performance, the model is ready to predict the five considered scenarios. The obtained results are presented in Fig. 15.

Based on the presented results, the most effective predicted results can be found by WOA compared with the actual crack length using different inputs. For better evaluation, the errors between exact and predicted crack length for all scenarios using various optimizations techniques are presented in Fig. 16.

Table 5 summarized the results of three inputs (strain-stress- displacement) compared with actual crack length, including errors between actual and predicted. Thus, the CPU times are computed for each scenario and shown in Table 6.

The obtained results demonstrate the effectiveness of the used optimization techniques. First, a critical observation was made from the results using GA-1 using different inputs. Furthermore, the results are improved after increasing the population size (GA-2 (2000 populations)).

The best computational time can be found in WOA and AOA between 75 and 95 s compared with significant differences in WOABAT and GA- 2.

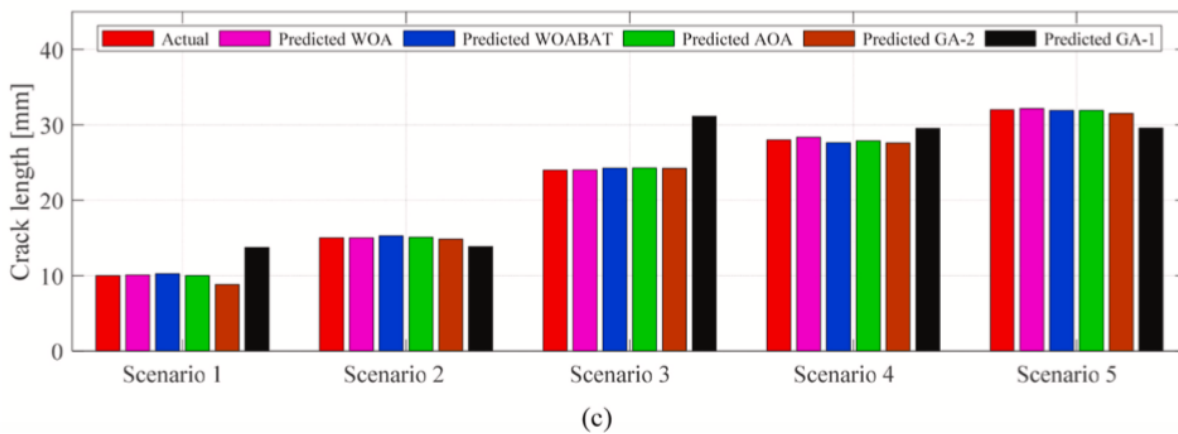
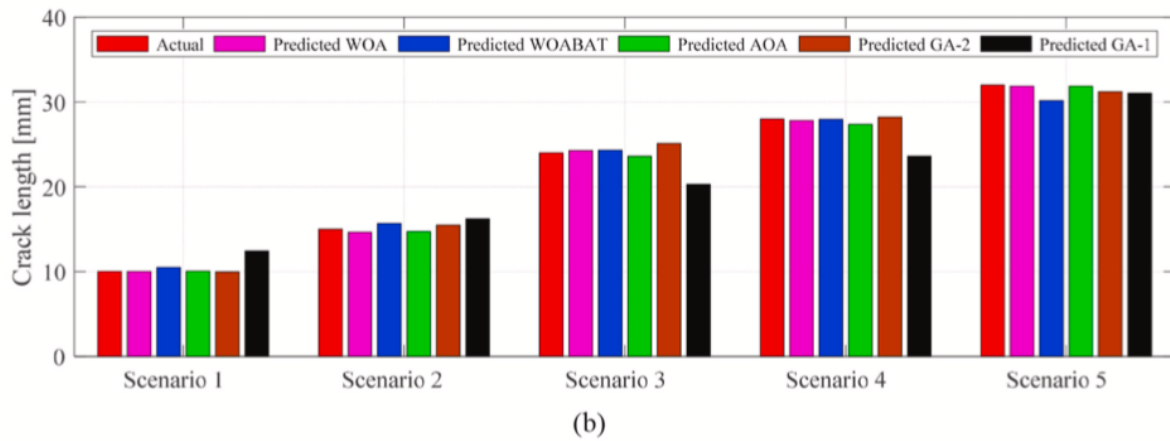
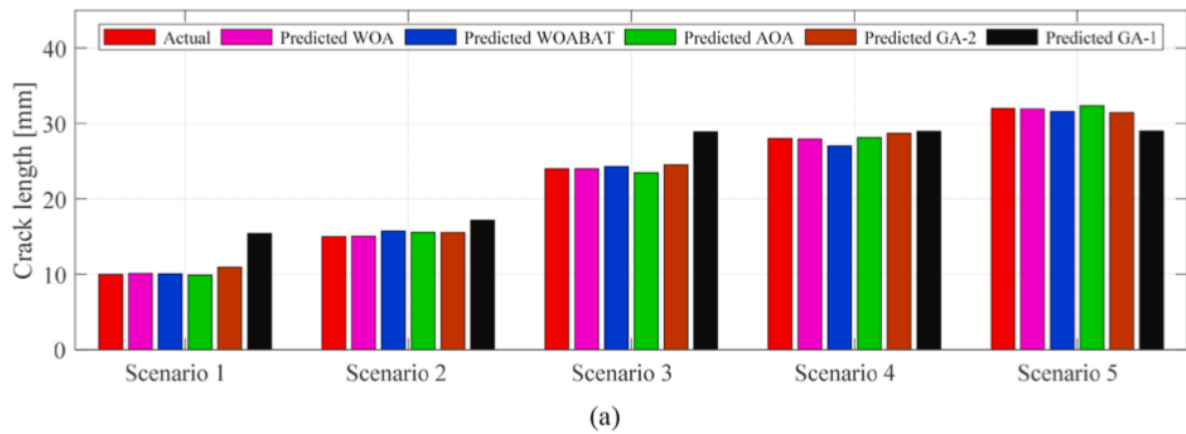
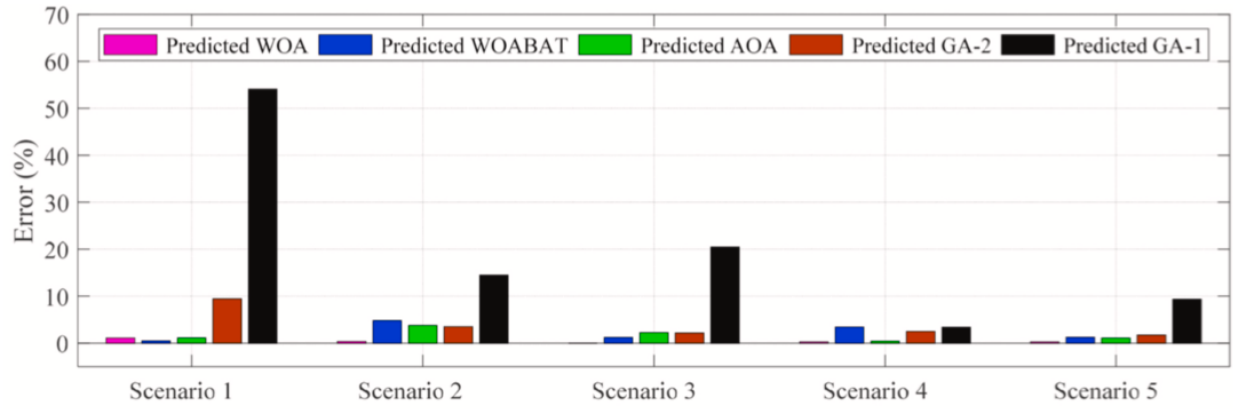
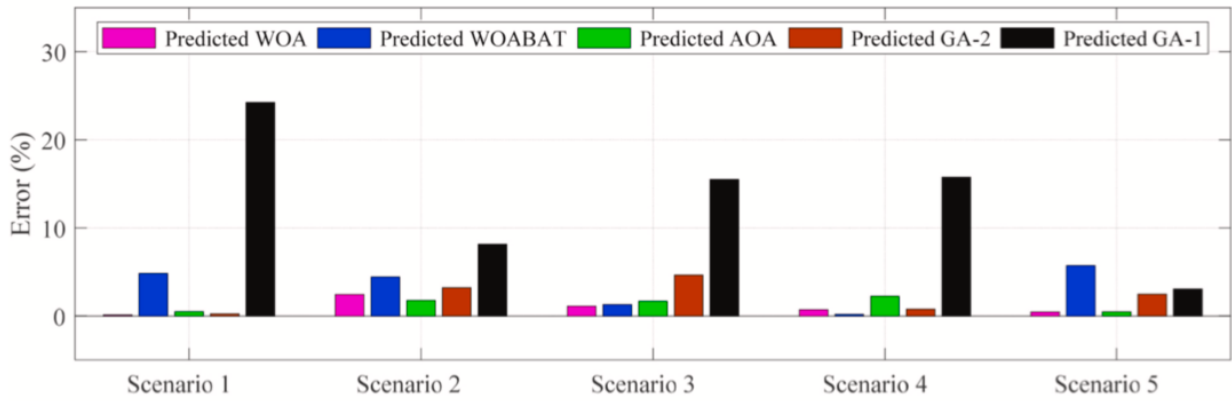


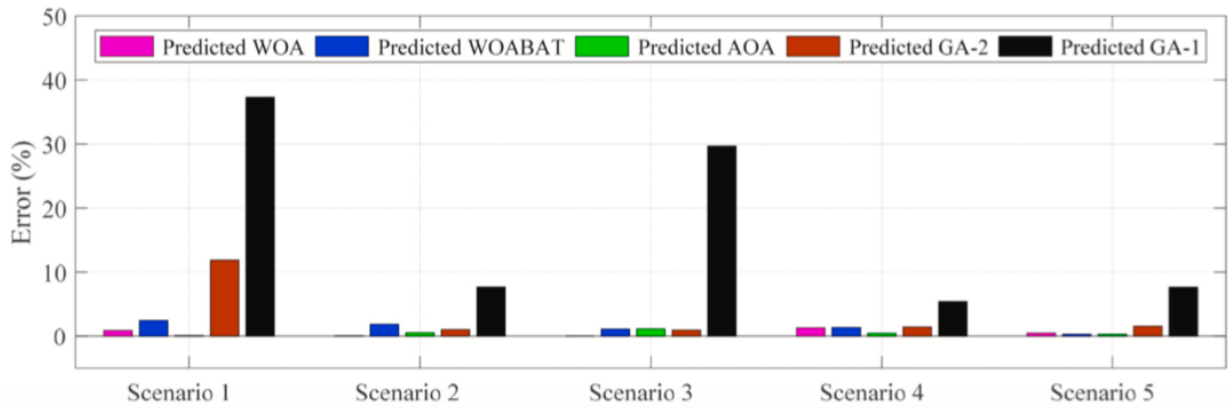
Figure 15 - Predicted crack length using 61 collected databases; a-Displacement, b-Strain, c-Stress.



(a)



(b)



(c)

Figure 16 - Percentage error using 61 collected databases; a-Displacement, b-Strain, c-Stress.

Table 5 - Percentage error of predicted WOA, WOA-BAT, AOA, GA-1, and GA-2 for each crack length scenario.

Crack length	Optimization	Data inputs					
		Displacement	Error (%)	Strain	Error (%)	Stress	Error (%)
L = 10 mm	WOA	10.111	1.110	10.012	0.120	10.088	0.880
	WOABAT	10.050	0.500	10.483	4.830	10.244	2.440
	AOA	9.888	1.120	10.050	0.500	10.009	0.090
	GA-2	10.942	9.421	9.976	0.245	8.813	11.870
	GA-1	15.409	54.089	12.425	24.246	13.731	37.307
L = 15 mm	WOA	15.050	0.333	14.634	2.440	15.012	0.080
	WOABAT	15.721	4.807	15.666	4.440	15.278	1.853
	AOA	15.567	3.780	14.734	1.773	15.079	0.527
	GA-2	15.527	3.512	15.483	3.221	14.844	1.039
	GA-1	17.177	14.514	16.223	8.153	13.853	7.649
L = 24 mm	WOA	24.001	0.004	24.265	1.104	24.006	0.025
	WOABAT	24.289	1.204	24.310	1.292	24.265	1.104
	AOA	23.464	2.233	23.599	1.671	24.276	1.150
	GA-2	24.521	2.172	25.116	4.650	24.229	0.955
	GA-1	28.908	20.452	20.281	15.494	31.121	29.671
L = 28 mm	WOA	27.928	0.257	27.801	0.711	28.358	1.279
	WOABAT	27.042	3.421	27.947	0.189	27.627	1.332
	AOA	28.121	0.432	27.373	2.239	27.878	0.436
	GA-2	28.692	2.470	28.218	0.780	27.596	1.444
	GA-1	28.954	3.405	23.590	15.751	29.509	5.391
L = 32 mm	WOA	31.918	0.256	31.856	0.450	32.151	0.472
	WOABAT	31.595	1.266	30.166	5.731	31.900	0.313
	AOA	32.351	1.097	31.846	0.481	31.907	0.291
	GA-2	31.442	1.744	31.208	2.476	31.504	1.551
	GA-1	29.005	9.359	31.021	3.060	29.557	7.633

Table 6 - CPU time of WOA, WOA-BAT, AOA, and GA for each crack length scenario.

Crack length	Optimization	CPU Time based on different database inputs (Sec)		
		Displacement	Strain	Stress
L = 10 mm	WOA	80.9837	94.9460	87.8769
	WOABAT	2288.975006	2499.596441	2726.764726
	AOA	80.6388	85.0736	78.0631
	GA-2	3038.0734	3167.739	3082.5555
	GA-1	156.58166	155.37554	163.83296
L = 15 mm	WOA	85.8602	83.7848	84.2638
	WOABAT	2713.802802	2433.929142	2797.347175
	AOA	85.8118	76.3816	75.0310
	GA-2	3189.2067	3050.9033	3084.3608
	GA-1	163.45587	171.36059	160.12588
L = 24 mm	WOA	82.1883	85.4778	80.7935
	WOABAT	2196.416295	2411.864277	2879.339001
	AOA	75.4474	78.5609	81.2045
	GA-2	2956.2631	2949.6275	3185.1473
	GA-1	148.49252	154.43498	160.82294
L = 28 mm	WOA	87.0286	75.0774	87.2644
	WOABAT	2044.215224	2814.371634	3327.286624
	AOA	75.9095	78.2227	80.6060
	GA-2	2872.9348	3202.2556	3290.9627
	GA-1	152.56876	176.48117	162.28916
L = 32 mm	WOA	82.1251	75.9302	83.6858
	WOABAT	1995.307727	2314.740854	3254.794972
	AOA	76.9729	78.1226	83.6941
	GA-2	2856.5266	3105.268	3345.6769
	GA-1	157.83188	170.99801	163.864

7. Conclusion

A comprehensive analysis was done for the development of hybrid ANN with optimization techniques to predict crack length using different parameters (Hidden layer neurons, bias, and weight). Recently developed optimization techniques are used to improve ANN for better prediction compared with other approaches to describe the effectiveness of the presented method. Different inputs such as strains, stresses, and displacements are compared using WOA, GA, AOA, and WOA-BAT. Numerical and experimental tests are investigated for validation in both cases of uncracked and cracked specimens. After validating the model, different crack lengths are supposed to build a database. The following observations have been reached based on this study:

- The Artificial Neural Network (ANN) with eight neurons in the hidden layer is the most optimum network in all optimization techniques.
- GA has a critical result with less population and generation (100-100).
- The best CPU time found by WOA and AOA compared with GA and WOA-BAT.

Acknowledgement

This work was funded by Vingroup Joint Stock Company and supported by Vingroup Innovation Foundation (VINIF) under project code VINIF.2021.DA00192.

ABBREVIATIONS

GA, Genetic Algorithm;
WOA, Whale Optimization Algorithm;
AOA, Arithmetic Optimization Algorithm;
WOABAT, Hybrid WOA Bat Algorithm;
ASTM, American Society for Testing and Materials;
GTN, Gurson-Tvergaard-Needleman.

References

- Aldakheel, F., Wriggers, P., Miehe, C., 2018. A modified Gurson-type plasticity model at finite strains: formulation, numerical analysis and phase-field coupling. *Comput. Mech.* 62 (4), 815–833.
- Antolovich, S.D., Saxena, A., Gerberich, W.W., 2018. Fracture mechanics – an interpretive technical history. *Mech. Res. Commun.* 91, 46–86.
- Bott, I.d.S., et al., 2005. High-strength steel development for pipelines: a brazilian perspective. *Metall. Mater. Trans.* 36 (2), 443–454.
- Bouledroua, O., et al., 2017. Effect of sandblasting on tensile properties, hardness and fracture resistance of a line pipe steel used in Algeria for oil transport. *J. Fail. Anal. Prev.* 17 (5), 890–904.
- Brahme, A., Winning, M., Raabe, D., 2009. Prediction of cold rolling texture of steels using an Artificial Neural Network. *Comput. Mater. Sci.* 46 (4), 800–804.
- Broek, D., 2012. *Elementary Engineering Fracture Mechanics*. Springer Science & Business Media.
- Cabrini, M., et al., 2015. Environmentally assisted cracking and hydrogen diffusion in traditional and high-strength pipeline steels. *Corrosion Rev.* 33 (6), 529–545.
- Capozucca, R., Magagnini, E., 2018. Experimental vibration response of homogeneous beam models damaged by notches and strengthened by CFRP lamina. *Compos. Struct.* 206, 563–577.
- Capozucca, R., Magagnini, E., 2020. RC beam models damaged and strengthened with GFRP strips under bending loading and free vibration. *Compos. Struct.* 253, 112730.
- Contreras, A., et al., 2005. Slow strain rate corrosion and fracture characteristics of X-52 and X-70 pipeline steels. *Materials Science and Engineering: A* 407 (1), 45–52.
- Cruse, T.A., 2012. *Boundary Element Analysis in Computational Fracture Mechanics*, vol. 1. Springer Science & Business Media.
- Fang, J., Zhang, J.-w., Huang, X., 2015. Industrial application of Instrumented DWTT in evaluating material resistance to ductile fracture for modern pipeline steels. In: *EPJ Web of Conferences*, p. 94.
- François, D., Pineau, A., Zaoui, A., 2012. *Mechanical Behaviour of Materials: Volume II: Fracture Mechanics and Damage*, vol. 191. Springer Science & Business Media.
- Gholipour, H., Biglari, F.R., Nikbin, K., 2019. Experimental and numerical investigation of ductile fracture using GTN damage model on in-situ tensile tests. *Int. J. Mech. Sci.* 164, 105170.
- Han, S.Y., et al., 2012. Effects of microstructure and yield ratio on strain hardening and Bauschinger effect in two API X80 linepipe steels. *Materials Science and Engineering: A* 551, 192–199.
- Hertzberg, R.W., Vinci, R.P., Hertzberg, J.L., 2020. *Deformation and Fracture Mechanics of Engineering Materials*. John Wiley & Sons.
- Jackiewicz, J., 2011. Use of a modified Gurson model approach for the simulation of ductile fracture by growth and coalescence of microvoids under low, medium and high stress triaxiality loadings. *Eng. Fract. Mech.* 78 (3), 487–502.

- Jang, Y.-Y., et al., 2019. Evaluations of ductile and cleavage fracture using coupled GTN and beremin model in API X70 pipelines steel. In: ASME 2019 38th International Conference on Ocean, Offshore and Arctic Engineering.
- Jiang, W., Li, Y., Su, J., 2016. Modified GTN model for a broad range of stress states and application to ductile fracture. *Eur. J. Mech. Solid.* 57, 132–148.
- Khalaj, G., Khoeini, M., Khakian-Qomi, M., 2013. ANN-based prediction of ferrite fraction in continuous cooling of microalloyed steels. *Neural Comput. Appl.* 23 (3), 769–777.
- Khatir, S., et al., 2020. An efficient hybrid TLBO-PSO-ANN for fast damage identification in steel beam structures using IGA. *Smart Struct. Syst.* 25 (5), 605–617. Khatir, S., et al., 2021. An improved Artificial Neural Network using Arithmetic Optimization Algorithm for damage assessment in FGM composite plates. *Compos. Struct.* 273, 114287.
- Li, J., et al., 2015. Numerical simulation of incremental sheet forming based on GTN damage model. *Int. J. Adv. Manuf. Technol.* 81 (9), 2053–2065.
- Lian, Y.D., et al., 2018. Application of GTN Model in tensile Fracture of pipeline steel. *Key Eng. Mater.* 777, 451–456.
- Mirjalili, S., Lewis, A., 2016. The whale optimization algorithm. *Adv. Eng. Software* 95, 51–67.
- Mohtadi-Bonab, M.A., Szpunar, J.A., Razavi-Tousi, S.S., 2013. Hydrogen induced cracking susceptibility in different layers of a hot rolled X70 pipeline steel. *Int. J. Hydrogen Energy* 38 (31), 13831–13841.
- Nakai, H., Shibamura, K., Aihara, S., 2016. Numerical model for unstable ductile crack propagation and arrest in pipelines using finite difference method. *Eng. Fract. Mech.* 162, 179–192.
- Nilsson, K.-F., Jakšić, N., Vokál, V., 2010. An elasto-plastic fracture mechanics based model for assessment of hydride embrittlement in zircaloy cladding tubes. *J. Nucl. Mater.* 396 (1), 71–85.
- Noell, P.J., Carroll, J.D., Boyce, B.L., 2018. The mechanisms of ductile rupture. *Acta Mater.* 161, 83–98.
- Ouladbrahim, A., et al., 2021a. Prediction of Gurson damage model parameters coupled with hardening law identification of steel X70 pipeline using neural network. *Met. Mater. Int.*
- Ouladbrahim, A., et al., 2021b. Sensitivity analysis of the GTN damage parameters at different temperature for dynamic fracture propagation in X70 pipeline steel using neural network. *Frat. Ed. Integrita` Strutt.* 15 (58), 442–452.
- Ozel, T., Karpat, Y., 2005. Predictive modeling of surface roughness and tool wear in hard turning using regression and neural networks. *Int. J. Mach. Tool Manufact.* 45 (4), 467–479.
- Rudland, D.L., et al., 2004. Characterizing dynamic fracture toughness of linepipe steels using the pressed-notch drop-weight-tear test specimen. *Eng. Fract. Mech.* 71 (16), 2533–2549.
- Seguini, M., et al., 2021. Crack prediction in pipeline using ANN-PSO based on numerical and experimental modal analysis. *Smart Struct. Syst.* 27, 507.

- Sha, Q., Li, D., 2016. Microstructure and properties of low manganese API X70 pipeline steel for sour service application. In: Proceedings of the 8th Pacific Rim International Congress on Advanced Materials and Processing. Springer International Publishing, Cham.
- Shi, X., et al., 2016. Novel Cu-bearing high-strength pipeline steels with excellent resistance to hydrogen-induced cracking. *Mater. Des.* 92, 300–305.
- Sun, W., et al., 2002. Influence of Nb, V and Ti on peak strain of deformed austenite in Mo-based micro-alloyed steels. *J. Mater. Process. Technol.* 125–126, 72–76.
- Xie, F., et al., 2021. Stress corrosion cracking behavior induced by Sulfate-reducing bacteria and cathodic protection on X80 pipeline steel. *Construct. Build. Mater.* 308, 125093.
- Xue, L., 2007. Ductile Fracture Modeling: Theory, Experimental Investigation and Numerical Verification. Massachusetts institute of technology.
- Zenzen, R., et al., 2020. A modified transmissibility indicator and Artificial Neural Network for damage identification and quantification in laminated composite structures. *Compos. Struct.* 248, 112497.
- Zhong, Y., et al., 2006. In situ TEM study of the effect of M/A films at grain boundaries on crack propagation in an ultra-fine acicular ferrite pipeline steel. *Acta Mater.* 54 (2), 435–443.